Research Square

Preprints are preliminary reports that have not undergone peer review.
They should not be considered conclusive, used to inform clinical practice,
or referenced by the media as validated information.

Emerging network model in a twisted monolayer--rhombohedral graphene

Juyoung Song
Konkuk University
Jeyong Park
Max Planck Institute for Solid State Research
Jinhong Park
jinhongpark@konkuk.ac.kr

Konkuk University

Research Article

Keywords:

Posted Date: August 13th, 2026

DOI: https://doi.org/10.21203/rs.3.rs-10538711/v1

License: This work is licensed under a Creative Commons Attribution 4.0 International License.
Read Full License

Additional Declarations: No competing interests reported.

Emerging network model in a twisted monolayer–rhombohedral graphene

Juyoung Song,[1] Jeyong Park,[2,3] and Jinhong Park[1]

[1] *Department of Physics, Konkuk University, Seoul 05029, Republic of Korea*
[2] *Max Planck Institute for Solid State Research, D-70569 Stuttgart, Germany*
[3] *School of Natural Sciences, Technische Universität München, D-85748 Garching, Germany*

(Dated: July 30, 2026)

We investigate the coexistence of localized states and propagating one-dimensional (1D) modes in graphene moiré systems. We first show within a minimal model that a spatially varying scalar potential can confine localized states, while sign changes of a staggered potential generate 1D modes along the resulting domain walls. These two types of states can coexist within the same finite energy window and form a hybrid network. We then demonstrate a microscopic realization of this mechanism in twisted monolayer–rhombohedral N-layer graphene. Band structures, energy contours, and Bloch wave functions obtained in a realistic parameter regime reveal the coexistence of localized nearly flat-band states and propagating quasi-1D modes. Our results establish twisted monolayer–rhombohedral graphene as a promising platform for realizing hybrid electronic networks with coexisting states of distinct effective dimensionalities.

I. INTRODUCTION

Moiré materials formed by stacking van der Waals layers with a small lattice mismatch or relative twist provide a versatile platform for engineering electronic band structures and correlated quantum phases [1, 2]. A prototypical example is twisted bilayer graphene (TBG), in which nearly flat bands emerge near the charge-neutrality point at the magic angle $\theta \simeq 1.1^\circ$ [3–5]. The interaction effects enhanced by these flat bands give rise to a wide variety of correlated and topological phases [6–10]. More recently, rhombohedral multilayer graphene and its moiré heterostructures have emerged as a complementary graphene platform with highly tunable surface flat bands and correlated topological states, including integer and fractional Chern insulators [11–34]. In particular, twisted monolayer–rhombohedral N-layer graphene has recently been experimentally realized for several layer numbers and shown to host a layer-tunable hierarchy of high-Chern-number orbital and quantum anomalous Hall states [12, 35, 36].

Besides generating flat bands, moiré structures can spatially modulate local band gaps and thereby create networks of one-dimensional (1D) electronic channels. In electrically biased, minimally twisted bilayer graphene, for example, the AB- and BA-stacked regions carry opposite valley Hall indices, and their domain walls support valley-protected 1D modes [37–41]. The interacting physics of such domain-wall structures has been investigated using quantum-wire and bosonized network descriptions [42, 43]. Related mechanisms for forming and controlling 1D topological channels have also been studied in heterostrained and minimally twisted bilayer graphene [44, 45]. These studies demonstrate that moiré materials can host electronic structures whose effective dimensionality is lower than that of the underlying two-dimensional system.

In our previous work [46], we showed that a single layer of graphene subject to smooth scalar and staggered moiré potentials can host an unusual coexistence of nearly localized states and propagating 1D channels within the same finite energy window. The staggered potential locally opens a gap in graphene, and its sign changes generate valley-resolved chiral modes along the resulting domain walls. At the same time, the scalar potential confines additional states near the junctions of the domain-wall network, giving rise to nearly flat bands. The resulting low-energy degrees of freedom form a hybrid network consisting of localized modes connected by propagating 1D channels. In the present work, we extend this framework to twisted monolayer–rhombohedral N-layer graphene and demonstrate that the coexistence of localized states and propagating 1D modes can also arise in this realistic moiré system.

In this work, we show that twisted monolayer–rhombohedral N-layer graphene provides a microscopic realization of this mechanism. We first revisit the minimal monolayer model to clarify how the spatially modulated scalar and staggered potentials generate, respectively, localized states and 1D domain-wall modes. We then derive an effective moiré Hamiltonian for the monolayer graphene by integrating out the electrically gapped rhombohedral graphene. When the characteristic decay length of the rhombohedral Green function is much shorter than the moiré period, the resulting nonlocal self-energy reduces to a local Hamiltonian of the same form as the minimal model. From the band structures, energy contours, and Bloch wave functions, we demonstrate that in a realistic parameter regime, localized nearly flat-band states coexist with propagating quasi-1D modes, thereby forming a hybrid network.

Our results establish twisted monolayer–rhombohedral graphene as a promising platform for realizing a hybrid electronic network with coexisting localized and propagating degrees of freedom. Such a system provides a microscopic starting point for interacting network models in which the 1D channels mediate coupling between localized spin-, valley-, and orbital degrees of freedom as studied in Ref. [46].

II. TOY MODEL: A GRAPHENE ON A TRIANGLE SUBLATTICE WITH TWIST

We consider a toy model of monolayer graphene placed on a triangular substrate, with a relative twist angle θ between the graphene and the substrate. The substrate lattice is assumed to have the same lattice constant a as the graphene lattice. The twist produces a spatially varying relative displacement between the two layers, resulting in the moiré pattern illustrated in Fig. 1(a). The local stacking configurations within a moiré unit cell are labeled by $\alpha\beta$, where the labels A and B (represented by filled red and blue circles, respectively) denote the two graphene sublattices, while C (empty circles) denotes the hollow site at the center of a graphene hexagon. For the triangular substrate, A denotes an atomic site and C denotes a hollow position. The notation $\alpha\beta$ indicates that sublattice $\alpha \in \{A, B, C\}$ of the graphene layer lies directly above sublattice $\beta \in \{A, C\}$ of the substrate. The three local staking configurations, AA, BA and AC, are shown in Fig. 1(a).

For this moiré configuration, we consider a potential model in which the graphene layer is subject to an electrostatic potential induced by the triangular substrate. We assume that there is no direct hopping or hybridization between the graphene and substrate. Neglecting the spin degree of freedom, the effective low-energy Hamiltonian of graphene in real space is given by

$$H_0(\boldsymbol{r}) = -iv_F(\sigma_x\tau_z\partial_x + \sigma_y\tau_0\partial_y) + V_0(\boldsymbol{r})\mathbb{1} + V_s(\boldsymbol{r})\sigma_z\tau_0\,. \tag{1}$$

Here, the Pauli matrices τ_i and σ_i act in the valley and sublattice spaces, respectively, and v_F is the Dirac velocity of graphene. The staggered potential $V_s(\boldsymbol{r})$ and scalar potential $V_0(\boldsymbol{r})$ are defined as the difference and sum, respectively, of the potentials [$V_A(\boldsymbol{r})$ and $V_B(\boldsymbol{r})$] acting on the A and B sublattices of graphene:

$$V_s(\boldsymbol{r}) \equiv \frac{V_A(\boldsymbol{r}) - V_B(\boldsymbol{r})}{2}\,, \qquad V_0 \equiv \frac{V_A(\boldsymbol{r}) + V_B(\boldsymbol{r})}{2} \tag{2}$$

The staggered potential V_s locally opens a mass gap in the Dirac spectrum, whereas the scalar potential V_0 produces a local energy shift.

At a small twist angle, the local stacking configuration varies smoothly over the moiré length scale. Consequently, the induced potentials $V_A(\mathbf{r})$ and $V_B(\mathbf{r})$, and hence $V_0(\mathbf{r})$ and $V_s(\mathbf{r})$, are also smooth functions of position $\boldsymbol{r}$. The smoothness of the potentials allows us to expand V_α with the lowest Fourier components:

$$V_\alpha(\boldsymbol{r}) = \overline{V}_\alpha + \sum_{\beta=A,C}\sum_{i=1}^{6} u_{\alpha\beta}e^{i\boldsymbol{G}_i\cdot(\boldsymbol{r}-\boldsymbol{r}_{\alpha\beta})}\,, \tag{3}$$

with $\alpha \in \{A, B\}$. Here $\boldsymbol{G}_i$ $(i = 1, \cdots, 6)$ are the six shortest nonzero reciprocal lattice vectors of the moiré superlattice with $|\boldsymbol{G}_i| = G = \frac{4\pi}{\sqrt{3}L}$ and L is the moiré lattice constant. The vectors $\boldsymbol{r}_{\alpha\beta}$ denote the positions of the corresponding local stacking configurations: $\boldsymbol{r}_{AA} = \boldsymbol{r}_{BC} = \boldsymbol{0}$ and $\boldsymbol{r}_{AC} = -\boldsymbol{r}_{BA} = (\frac{\sqrt{3}L}{6}, \frac{L}{2})^T$. The parameters $u_{\alpha\beta}$ represent the amplitudes of the first moiré harmonics associated with the local stacking configurations $\alpha\beta$.

As a minimal parametrization, we neglect lattice-relaxation-induced corrugation and assume

$$u_{AA} = u_{BA} = u_0, \qquad u_{AC} = u_{BC} = 0. \tag{4}$$

We also neglect the spatially uniform components $\overline{V}_\alpha$ by assuming that the A and B sublattices of graphene experience the same potential on average over a moiré unit cell. Under this assumption, the uniform staggered potential $\overline{V}_s \equiv (\overline{V}_A - \overline{V}_B)/2$ vanishes, while the remaining uniform scalar potential $\overline{V}_0 \equiv (\overline{V}_A + \overline{V}_B)/2$ can be absorbed into the chemical potential. However, when we consider a more realistic system in Sec. III, we will show that $\overline{V}_s$ becomes finite and has to be included explicitly.

The staggered and scalar potentials [Eq. (2)] are plotted in Fig. 1(b). The staggered potential $V_s(\boldsymbol{r})$ shown in the left panel of Fig. 1(b) vanishes along the green lines and changes sign across them. According to the Jackiw–Rebbi mechanism [47], each mass domain wall supports a 1D chiral gapless mode for each valley. The modes originating from the K and K' valleys propagate in opposite directions, forming a pair of counter-propagating valley-polarized modes. For a moiré system with a large moiré period L, the potentials vary smoothly on the moiré scale and therefore strongly suppress inter-valley scattering. Consequently, the two spatially overlapping 1D modes remain approximately decoupled.

At the same time, the scalar potential $V_0(\boldsymbol{r})$ (the right panel) has a minimum value at the AC region where the 1D domain-wall modes meet. The quadratic scalar potential near the AC region confines electrons, which may lead to localized modes at the junction.

These observations on the staggered and scalar potentials suggest an effective network model in which propagating 1D domain-wall modes coexist and couple with localized modes at the junctions. The emergence of such a network model was discussed in Ref. [46]. The present network model shares the same structure as that of Ref. [46], but it is shifted by $\boldsymbol{r} \to \boldsymbol{r} + \boldsymbol{r}_{AC}$ compared with that of Ref. [46].

The low-energy band structure of this toy model can be obtained using the approach first developed in Ref. [3]. To this end, we Fourier transform Hamiltonian (1) to the momentum space and diagonalize the resulting Hamiltonian. The band structure in the K valley is plotted along the high-symmetry path K–M–Γ–K of the monolayer graphene in Fig. 1(c). The bands fall into two classes: 1D bands (denoted as green lines) and flat bands (red lines). We now investigate these bands by inspecting the constant-energy contour of the bands and the Bloch wave function.

The constant-energy contours of the three 1D bands are shown in Fig. 1(d): 53, 55, and 56th bands (green lines in Fig. 1(c)) are displayed from the left to the right

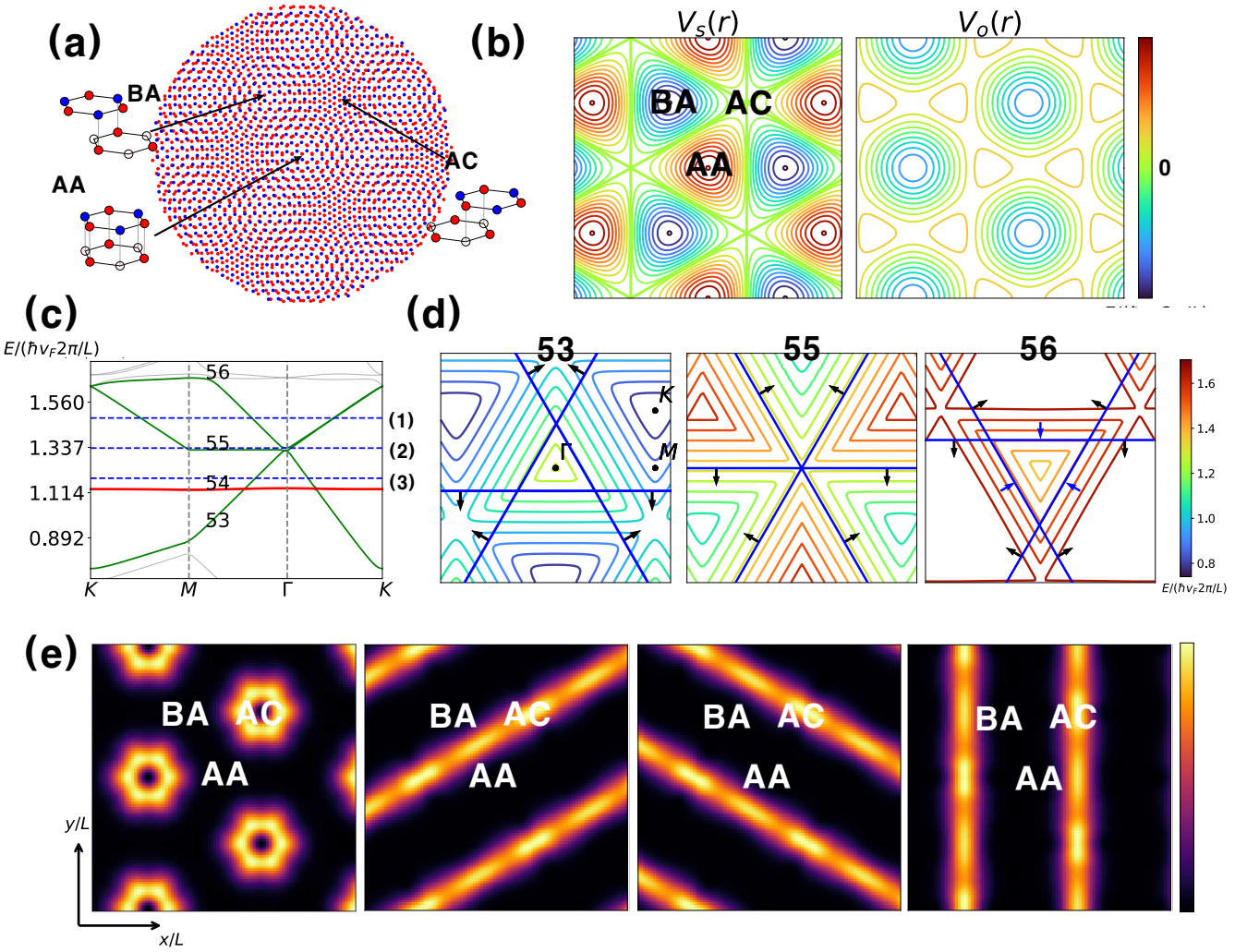


Figure 1. **Potential model**. **(a)** Moiré pattern from a graphene stacked on a triangular-lattice substrate with the same lattice constant as the graphene. A relative twist between graphene and the substrate produces a spatially varying displacement between the layers, generating local stacking patterns, BA, AC, AA. (b) Spatial profiles of the staggered potential $V_s(\boldsymbol{r})$ and scalar potential $V_0(\boldsymbol{r})$. The green lines in the left panel indicate the contours $V_s(\boldsymbol{r}) = 0$, along which the mass changes sign. The scalar potential has local minima at the AC regions, where the domain-wall modes meet. (c) Low-energy band structure along the high-symmetric path, $K - M - \Gamma - K$ near the K valley. The green and red curves denote the 1D and flat bands, respectively. (d) Constant-energy contours of the 53, 55, and 56 bands from left to right. The blue straight lines represent the ideal, decoupled 1D bands, and the black arrows indicate the directions in which the constant-energy contours move with increasing energy. The blue arrows mark the momenta selected for the real-space probability distributions in (e), while their orientations indicate the corresponding group-velocity directions. The high-symmetric momentum points, Γ, K, and M are marked in the plot for the 53th band. (e) Real-space probability distributions of selected Bloch states. The leftmost panel shows the flat-band state at the K point, whereas the three right panels show states in the 56 band at the momenta marked by the blue arrows in (d). The flat-band state is localized near an AC region, whereas the 1D-band states are extended along one direction and confined in the perpendicular direction.

panels of Fig. 1(d). The resulting contours have approximately equilateral triangular shapes centered at either the K or Γ point. The bands can be understood as 1D bands weakly coupled to each other. To see the 1D nature, we consider three ideal, decoupled 1D bands related by the C_{3z} rotational symmetry, as shown as the three green straight lines in each panel of Fig. 1(d). The three contours are evaluated at the energies indicated by the dashed lines labeled as (1), (2), and (3) in Fig. 1(c), respectively. In the decoupled 1D limit, the energy is independent of the momentum parallel to each straight line and disperses only in the perpendicular direction, as

indicated by the blue arrows. When a small coupling between them is induced, the bands hybridize near the three intersection points and develop avoided crossings, causing the constant-energy contours to separate and become rounded near these points. As shown in the constant-energy contours, such 1D bands with a small coupling emerge in our potential model. At the same time, the 54th band, shown in red, is nearly flat. The spectrum in the K' valley (not shown) is related to that in the K valley by time-reversal symmetry.

The features of these exotic bands can also be understood by inspecting the real-space probability distribution $P_{\boldsymbol{k}}(\boldsymbol{r}) = \sum_{\alpha=A,B} |\psi_{\boldsymbol{k},\alpha}|^2(\boldsymbol{r})$ of Bloch wave functions, as shown in Fig. 1(e). The leftmost panel of Fig. 1(e) represents $P_{\boldsymbol{k}}(\boldsymbol{r})$ for the flat band (54 band) at K point. As expected from the effective model, the wave function is highly localized in the AC region. The remaining three panels of Fig. 1(e) show $P_{\boldsymbol{k}}(\boldsymbol{r})$ for the 56th band at the three momenta marked by the blue arrows in Fig. 1(d): The orientation of each arrow indicates the group velocity at the corresponding momentum. The wave functions are extended along the corresponding group-velocity directions and confined in the perpendicular directions.

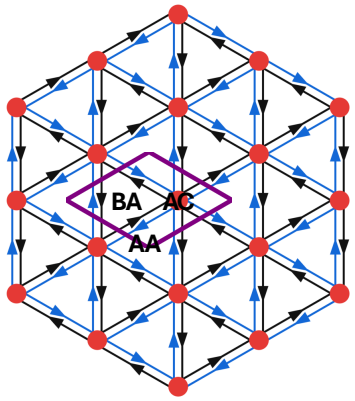


Figure 2. **Network model** emerging from the potential model presented in Fig. 1. Localized modes (denoted red nodes) in the AC region are connected by pairs of counterpropagating 1D modes. The blue and black arrows represent the chiral modes originating from the K and K' valleys, respectively, and indicate their propagation directions.

From the above discussions of the band structure, constant-energy contours, and Bloch wave functions, we conclude that an effective network model consisting of 1D domain-wall modes and localized modes emerges within a finite energy window; see figure 2. The nearly flat band is associated with states localized near the AC junctions, while the links of the network are formed by pairs of counterpropagating 1D modes originating from the K and K' valleys. The K-valley modes are explicitly demonstrated in Fig. 1, while the corresponding K'-valley modes follow from time-reversal symmetry. Consequently, the 1D modes in the two valleys propagate in opposite directions along each domain wall.

III. TWISTED MONOLAYER–RHOMBOHEDRAL N-LAYER GRAPHENE

So far, we have discussed a toy model in which an effective network consisting of 1D modes and localized modes emerges. As a possible platform for realizing this model, we consider twisted monolayer–rhombohedral N-layer graphene, which has recently been experimentally realized for several layer numbers [12, 35, 36]. In this system, monolayer graphene is placed on rhombohedral N-layer graphene with a relative twist angle. Compared with the toy model, the triangular substrate is replaced by rhombohedral graphene. A perpendicular displacement field is applied to open a gap in the low-energy spectrum of the rhombohedral graphene. When the energy lies well inside this gap, a real charge transfer between the monolayer and rhombohedral graphene is strongly suppressed. In this regime, the effect of the rhombohedral graphene on the monolayer can be described by an effective moiré potential, analogous to the potential model introduced in Sec. II.

The rhombohedral N-layer graphene consists of N layers of graphene with the stacking sequence $ACBA\cdots$. As in the toy model, we list the stacking sequence from the uppermost to the lowermost layer and adopt the anticyclic stacking convention for rhombohedral graphene. When monolayer graphene is stacked on the rhombohedral N-layer graphene with a relative twist angle θ, three high-symmetry local stacking configurations appear within a moiré unit cell: $AAC\cdots$, $BAC\cdots$, and $ABA\cdots$, as shown in Fig. 3(a). For brevity, we refer to these configurations as the AA, BA, and AB regions, respectively.

To capture the essential low-energy physics, we employ a continuum model following the approach developed in Ref. [3]. We consider an electric field applied perpendicular to the $N+1$ graphene layers. Assuming a linear potential drop across the layers, the electrostatic potential on the ith layer, counted from the uppermost layer, is taken to be

$$U_i = U\left[\frac{1}{2} - \frac{i-1}{N}\right], \qquad 1 \le i \le N+1. \tag{5}$$

Here U is the potential difference between the uppermost and lowermost layers. The total Hamiltonian in a continuum limit reads

$$H = \begin{pmatrix} H_{\mathrm{MLG}} & T \\ T^\dagger & H_{\mathrm{RHG}} \end{pmatrix}, \tag{6}$$

where H_{MLG} and H_{RHG} describe the monolayer graphene and the rhombohedral N-layer graphene, respectively, while T denotes the moiré tunneling between them. Near

the K valley, the monolayer Hamiltonian H_{MLG} in the sublattice basis is given by

$$H_{\mathrm{MLG}}(\boldsymbol{k}) = v_F \boldsymbol{k}_{\theta/2} \cdot \boldsymbol{\sigma} + \frac{U}{2}\mathbb{1}\,, \tag{7}$$

with the rotated momenta $\boldsymbol{k}_\theta \equiv R(\theta)\boldsymbol{k}$ by twist angle θ. Here $R(\phi)$ is the rotation matrix with angle ϕ, and $\boldsymbol{\sigma} = (\sigma_x, \sigma_y)$ are the Pauli matrices acting on the sublattice space. The rhombohedral N-layer graphene is described in the basis $(A_1, B_1, \ldots, A_N, B_N)$, where the indices $1, \ldots, N$ label the layers from top to bottom, by the following $2N \times 2N$ Hamiltonian:

$$H_{\mathrm{RHG}}(\boldsymbol{k}) = \begin{pmatrix} h_1(\boldsymbol{k}) & \Gamma & 0 & \cdots & 0 \\ \Gamma^\dagger & h_2(\boldsymbol{k}) & \Gamma & \ddots & \vdots \\ 0 & \Gamma^\dagger & h_3(\boldsymbol{k}) & \ddots & 0 \\ \vdots & \ddots & \ddots & \ddots & \Gamma \\ 0 & \cdots & 0 & \Gamma^\dagger & h_N(\boldsymbol{k}) \end{pmatrix}, \tag{8}$$

where the intralayer Hamiltonian of the jth layer is

$$h_j(\boldsymbol{k}) = v_F \boldsymbol{k}_{-\theta/2} \cdot \boldsymbol{\sigma} + U_{j+1}\mathbb{1}\,. \tag{9}$$

Since the rhombohedral block starts from the second layer of the full heterostructure, its jth layer experiences the potential U_{j+1}. For the anticyclic stacking sequence $ACBA\cdots$, the nearest-neighbor interlayer hopping is given by

$$\Gamma = \begin{pmatrix} 0 & 0 \\ \gamma & 0 \end{pmatrix}. \tag{10}$$

Here, γ denotes the nearest-neighbor interlayer hopping between A_{j+1} and B_j. In this minimal model, we neglect remote hopping processes and set the onsite-energy asymmetry Δ to zero; see Ref. [48] for the neglected parameters. However, we have checked that the inclusion of the neglected parameters does not qualitatively change the physics we discussed in the paper.

The moiré tunneling between the monolayer graphene and the uppermost layer of the rhombohedral graphene is described by the $2 \times (2N)$ matrix

$$T(\boldsymbol{r}) = \sum_{m=1}^{3} e^{i\boldsymbol{q}_m \cdot \boldsymbol{r}} T_m\,, \tag{11}$$

with

$$T_m = \begin{pmatrix} w_{AA} & w_{AB}e^{-i(m-1)\frac{2\pi}{3}} & 0 & 0 & \cdots & 0 & 0 \\ w_{AB}e^{i(m-1)\frac{2\pi}{3}} & w_{AA} & 0 & 0 & \cdots & 0 & 0 \end{pmatrix}, \tag{12}$$

with $m = 1, 2, 3$. Here, w_{AA} denotes the tunneling strength in the local AA stacking configuration, while w_{AB} denotes the tunneling strength in the AB and BA configurations. We retain the three dominant momentum-transfer processes [3]. The vectors $\boldsymbol{q}_m$ denote the three momentum transfers corresponding to the dominant interlayer tunneling processes; $\boldsymbol{q}_1 = q_\theta(0, 1)$, $\boldsymbol{q}_2 = q_\theta(-\frac{\sqrt{3}}{2}, -\frac{1}{2})$, $\boldsymbol{q}_3 = q_\theta(\frac{\sqrt{3}}{2}, -\frac{1}{2})$, and $q_\theta = \frac{8\pi \sin(\theta/2)}{3a} = \frac{4\pi}{3L}$, a is the lattice constant, and $L = \frac{a}{2\sin(\theta/2)}$ is the moiré lattice constant.

We now map the Hamiltonian (6) for the twisted monolayer–rhombohedral graphene into the effective Hamiltonian (1) for the graphene by using the second order perturbation theory (namely, the Schrieffer-Wolff transformation). When energy is inside the gap of the rhombohedral graphene, i.e., $U_{N+1} < E < U_2$ and $w_{AA}, w_{AB} \ll |U_2 - U_{N+1}|$, the direct hybridization with the rhombohedral graphene is not allowed. Then, the leading correction to the monolayer Hamiltonian, (7), comes from the second-order process in tunneling, resulting in the effective Hamiltonian for the monolayer graphene,

$$(H_{\mathrm{eff}})_{\boldsymbol{k}\boldsymbol{k}'} \approx H_{\mathrm{MLG}}\delta_{\boldsymbol{k}\boldsymbol{k}'} + (\Delta H_{\mathrm{MLG}})_{\boldsymbol{k}\boldsymbol{k}'}\,, \tag{13a}$$

$$(\Delta H_{\mathrm{MLG}})_{\boldsymbol{k}\boldsymbol{k}'} = \sum_{m,m'=1,2,3} T_m \frac{1}{E - H_{\mathrm{RHG}}} T^\dagger_{m'} \delta_{\boldsymbol{k}', \boldsymbol{k}+\boldsymbol{q}_m - \boldsymbol{q}_{m'}}\,. \tag{13b}$$

Transforming into the real space, the second term of Eq. (13) becomes

$$\Delta H_{\mathrm{MLG}}(\boldsymbol{r}, \boldsymbol{r}') = T(\boldsymbol{r}) g_{\mathrm{RHG}}(E; \boldsymbol{r} - \boldsymbol{r}') T^\dagger(\boldsymbol{r}')\,, \tag{14}$$

where $g_{\mathrm{RHG}}(E; \boldsymbol{r} - \boldsymbol{r}') = (E - H_{\mathrm{RHG}})^{-1}(\boldsymbol{r} - \boldsymbol{r}')$ is the bare Green function of the rhombohedral graphene in real space.

Since the energy E lies inside the gap of the rhombohedral graphene, the Green function $g_{\mathrm{RHG}}(E; \boldsymbol{r} - \boldsymbol{r}') \sim e^{-|\boldsymbol{r}-\boldsymbol{r}'|/\xi}$ decays at large $|\boldsymbol{r}-\boldsymbol{r}'|$. Its decay length is given by $\xi \equiv 1/|\,\mathrm{Im}[\boldsymbol{k}_0]|$, where $\boldsymbol{k}_0$ is the complex-momentum solution with the smallest $|\mathrm{Im}[\boldsymbol{k}]|$ among those satisfying

$$\det\left[E - H_{\mathrm{RHG}}(\boldsymbol{k})\right] = 0. \tag{15}$$

Solving Eq. (15) with the rhombohedral graphene Hamiltonian (8), we find that in the regime of $U \ll \gamma$, ξ scales as

$$\xi \sim \frac{v_F}{\gamma^{1-\frac{1}{N}}\left[(U_2 - E)(E - U_{N+1})\right]^{\frac{1}{2N}}} \sim \frac{v_F}{\gamma(U/\gamma)^{1/N}}\,. \tag{16}$$

For sufficiently small twist angles, ξ is much smaller than L, and thus the nonlocal effect of $\Delta H_{\mathrm{MLG}}(\boldsymbol{r}, \boldsymbol{r}')$ can be neglected. We also note that, for $U \ll \gamma$, ξ decreases as N increases. The local approximation improves with increasing N.

In this local approximation, we can focus on $\Delta H_{\mathrm{MLG}}(\boldsymbol{r}, \boldsymbol{r})$ and map it onto the effective Hamiltonian as

$$H_{\mathrm{eff}}(\boldsymbol{r}) = v_F(-i\boldsymbol{\nabla}_{\boldsymbol{r}} - e\boldsymbol{A}(r)) \cdot \boldsymbol{\sigma} + V_0(\boldsymbol{r})\mathbb{1} + V_s(\boldsymbol{r})\sigma_z\,. \tag{17}$$

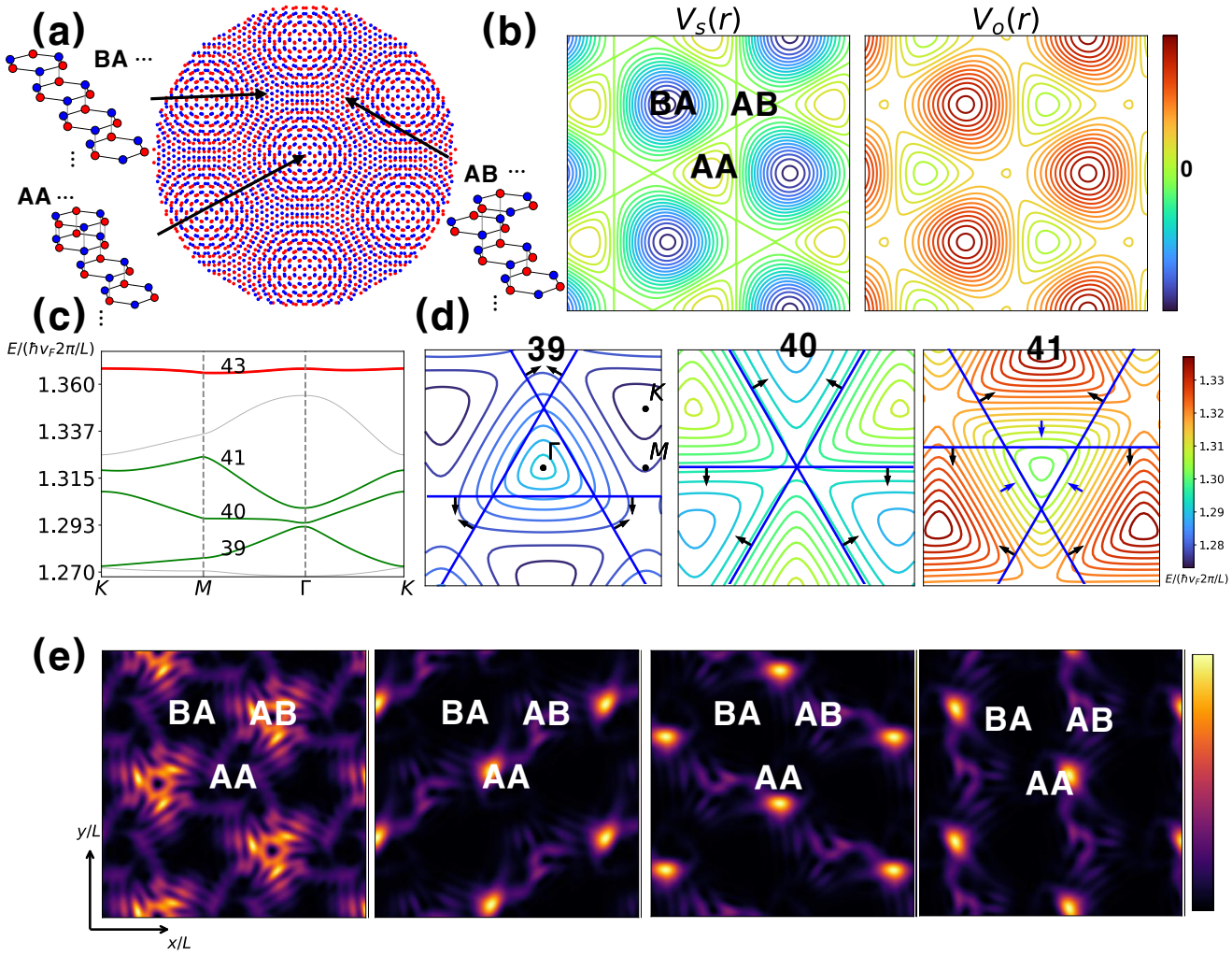


Figure 3. **Twisted rhombohedral–monolayer graphene**. **(a)** Schematic atomic structure of monolayer graphene twisted relative to an N-layer rhombohedral graphene. Red and blue circles denote the two sublattices, respectively. The enlarged side-views show the representative local AA, AB, and BA stacking configurations. **(b–e)** Results for $N = 3$. **(b)** Contour plots of the effective staggered potential $V_s(\boldsymbol{r})$ and scalar potential $V_0(\boldsymbol{r})$ induced in the monolayer graphene. The light-green contours indicate the domain walls defined by $V_s(\boldsymbol{r}) = 0$, which separate regions with opposite signs of the staggered potential. **(c)** Moiré band structure along the high-symmetry path K–M–Γ–K. The green and red bands identify the 1D and nearly flat bands, respectively. The four bands in the energy window of interest are labeled by their band indices 39–41 and 43. **(d)** Constant-energy contours of bands 39, 40, and 41 in the moiré Brillouin zone. The blue lines show the corresponding contours of an idealized 1D dispersion, providing a reference for the degree to which each band approaches the ideal 1D limit. The arrows indicate the directions of the group velocities, and the color scale represents the band energy. **(e)** Real-space probability densities of representative eigenstates. The leftmost panel shows an eigenstate of the nearly flat band 43 at the K point. The remaining three panels show eigenstates selected at momenta on the blue arrows in **(d)**. The parameters are $U = -200$ meV, $\gamma = 361$ meV, $w_{AA} = 55$ meV, $w_{AB} = 110$ meV, and $\theta = 0.181°$. Energies in **(c)** and **(d)** are expressed in units of $2\pi\hbar v_F/L$.

Here, we approximated $V_0(\boldsymbol{r}) \simeq \frac{1}{2}\mathrm{Tr}[H_{\mathrm{MLG}}(\boldsymbol{r},\boldsymbol{r})]$, $V_s(\boldsymbol{r}) \simeq \frac{1}{2}\mathrm{Tr}[H_{\mathrm{MLG}}(\boldsymbol{r},\boldsymbol{r})\sigma_z]$, and the effective vector potentials $\boldsymbol{A} = (A_x, A_y)$ where $A_l \simeq \frac{1}{2}\mathrm{Tr}[H_{\mathrm{MLG}}(\boldsymbol{r},\boldsymbol{r})\sigma_l]$ with $l = x, y$. We assumed that the twist angle θ is small and therefore neglect the θ-dependence in the first term of equation (17). We have checked that the effective magnetic field $\boldsymbol{B} = \boldsymbol{\nabla}_{\boldsymbol{r}} \times \boldsymbol{A}$ from the obtained vector potentials vanishes in every $\boldsymbol{r}$, and thus we can gauge away the vector potentials. Evaluating the scalar potential V_0 and staggered potential V_s from Eqs. (11), (13) and using Eq. (2), we show that V_A and V_B take the form as

$$V_A(\boldsymbol{r}) = \overline{V}_0 + \overline{V}_s + \sum_{\alpha=A,B}\sum_{i=1}^{6} u_{A\alpha} e^{i\boldsymbol{G}_i\cdot(\boldsymbol{r}-\boldsymbol{r}_{A\alpha})}, \quad \text{(18a)}$$

$$V_B(\boldsymbol{r}) = \overline{V}_0 - \overline{V}_s + \sum_{\alpha=A,B}\sum_{i=1}^{6} u_{B\alpha} e^{i\boldsymbol{G}_i\cdot(\boldsymbol{r}-\boldsymbol{r}_{B\beta})}, \quad \text{(18b)}$$

where we write the parameters $u_{\alpha\beta}$, $\overline{V}_0$ and $\overline{V}_s$,

$$u_{AA} = \frac{2N\omega_{AA}^2}{U(1-N)}, \quad u_{BA} = \frac{2N\omega_{AB}^2}{U(1-N)} \tag{19a}$$

$$u_{AB} = -\frac{2\omega_{AB}^2(N-3)NU}{\zeta}, \tag{19b}$$

$$u_{BB} = -\frac{2\omega_{AA}^2(N-3)NU}{\zeta} \tag{19c}$$

$$\overline{V}_s = \frac{3(\omega_{AA}^2-\omega_{AB}^2)(8N^3\gamma^2)}{2U(N-1)\zeta} \tag{19d}$$

$$\overline{V}_0 = \frac{3(\omega_{AB}^2+\omega_{AA}^2)(8N^3\gamma^2-4(N-3)(N-1)NU^2)}{2U(N-1)\zeta} \tag{19e}$$

with $\zeta = [(N-3)(N-1)U^2 - 4N^2\gamma^2]$. Here E is set to the middle of the gap, i.e., $E = (U_2 + U_{N+1})/2$.

In contrast to the toy model discussed in Sec. II, the uniform staggered potential is generally finite in the presence of lattice relaxation with $w_{AA} \neq w_{AB}$, owing to the inequivalence of the two surface sublattices of rhombohedral graphene. The terms with $m = m'$ in Eq. (13b) involve no momentum transfer within the monolayer graphene and therefore give the spatially uniform part of the effective potential. Its staggered component is given by

$$\overline{V}_s(\boldsymbol{k}) = \frac{1}{2}\,\mathrm{Tr}\,[\sigma_z(\Delta H_{\mathrm{MLG}})_{\boldsymbol{kk}}]\,. \tag{20}$$

Evaluating this expression shows that a finite uniform staggered potential requires two ingredients simultaneously: (i) the inequivalence of the two surface sublattices of the rhombohedral graphene and (ii) the tunneling anisotropy $w_{AA} \neq w_{AB}$. If $w_{AA} = w_{AB}$, the two monolayer sublattices couple to the inequivalent substrate channels with equal total weights, and their uniform energy shifts cancel to each other. Conversely, if sublattice symmetry were present in the rhombohedral graphene, the AB and BA configurations would be equivalent, and the A and B sublattices of graphene experience the same potential on average over a moiré unit cell even when $w_{AA} \neq w_{AB}$. Thus, the uniform staggered potential arises only from the combined effect of the substrate sublattice asymmetry and the tunneling anisotropy.

We now demonstrate that the coexistence of 1D and localized states found in the toy model also appears in a realistic twisted rhombohedral–monolayer graphene system. For concreteness, we consider $N = 3$ with $U = -200$meV, $\gamma = 361$meV, $w_{AA} = 55$meV, $w_{AB} = 110$meV, and $\theta = 0.181°$. Our choice of $w_{AA}/w_{AB} = 0.5$ is motivated by the suppression of the effective AA tunneling relative to the AB/BA tunneling found in relaxed small-angle graphene interfaces [49–51].

Figure 3(b) shows the resulting staggered and scalar potentials obtained from Eq. (18). Lattice relaxation generates a substantial uniform component $\overline{V}_s$, thereby shifting the zero contours of the total staggered potential $V_s(\boldsymbol{r})$. Nevertheless, the spatially varying components of the staggered potential remains sufficiently strong to produce sign changes near the AB region. The contours $V_s(\boldsymbol{r}) = 0$, shown in light-green lines, therefore form a network of domain walls along which 1D modes can emerge. At the same time, the scalar potential $V_0(\boldsymbol{r})$ develops extrema near the AB regions, suggesting the formation of localized modes there.

The corresponding moiré band structure is shown in Fig. 3(c). The bands near the energy window of interest contain both dispersive 1D bands, highlighted in green, and a nearly flat band, highlighted in red. To reveal their dimensional characteristics more directly, we plot in Fig. 3(d) the energy contours of bands 39–41. For an ideal 1D dispersion, the constant-energy contours form straight lines, shown in blue. Some of the calculated contours develop extended segments that follow these lines, demonstrating the emergence of quasi-1D propagation along the domain-wall network. This correspondence is particularly clear for band 40 and 41, whose contours closely approach those of the ideal 1D dispersion.

The real-space probability densities in Fig. 3(e) further confirm this interpretation. The leftmost panel shows a representative nearly flat-band state at the K point, whose probability density is concentrated near the AB regions. The remaining panels show states taken at three C_{3z}-related momenta on the 1D bands indicated by the blue arrows in Fig. 3(d). Their probability densities are concentrated along three directions of the domain-wall network, which intersects near the AB region. The enhanced probability weight near the junctions can be attributed to the reduced propagation velocity caused by strong hybridization among the intersecting 1D modes. These results demonstrate that the realistic twisted multilayer graphene system retains the characteristic coexistence of localized states and propagating 1D modes anticipated from the toy model.

IV. CONCLUSION AND OUTLOOK

In conclusion, we have shown that a van der Waals moiré heterostructure can host a hybrid electronic network in which localized states and quasi-1D modes coexist within a finite energy window. Within a minimal toy model, the scalar potential confines localized states, whereas sign changes of the staggered potential generate one-dimensional modes along the resulting domain walls. We further demonstrated that the same mechanism is realized in twisted monolayer–rhombohedral graphene. By integrating out the electrically gapped rhombohedral graphene, we derived an effective moiré Hamiltonian acting on the monolayer graphene, which reduces to the toy-model Hamiltonian. The calculated band dispersions, constant-energy contours, and real-space probability densities confirm the coexistence of localized states and propagating quasi-1D modes, establishing twisted monolayer–rhombohedral graphene as a realistic platform for realiz-

ing a network of electronic states with distinct effective dimensionalities.

The coexistence of localized states and propagating 1D channels also provides a promising setting for exploring interaction-driven phenomena beyond the single-particle physics studied here. When the coupling between the two sectors is weak, the 1D channels can mediate interactions between the localized spin and valley degrees of freedom, potentially stabilizing unconventional spin–valley orders, including states with nonzero scalar spin chirality, as discussed in Ref. [46]. At stronger coupling, the system may instead enter a Kondo-lattice regime in which the localized moments are dynamically screened by the 1D electronic modes. Since the latter are generically described as Luttinger liquids rather than Fermi liquids, their coupling to the localized moments may lead to unconventional quantum critical behavior and non-Fermi-liquid physics. Magnetic fluctuations associated with the localized degrees of freedom may further influence pairing tendencies in the propagating 1D channels, providing a possible route toward unconventional superconductivity. The hybrid network identified here therefore offers a versatile platform for investigating the interaction effects arising from the coupling between localized degrees of freedom and topological 1D modes.

ACKNOWLEDGEMENTS

J.Y.S and J.H.P acknowledge support from Korea NRF (Grant No. RS-2026-25492880). J.Y.P thanks the Kwanjeong Educational Foundation for support.

[1] A. K. Geim and I. V. Grigorieva, Van der Waals heterostructures, Nature 2013 499:7459 **499**, 419 (2013), arXiv:1307.6718.

[2] E. Y. Andrei, D. K. Efetov, P. Jarillo-Herrero, A. H. MacDonald, K. F. Mak, T. Senthil, E. Tutuc, A. Yazdani, and A. F. Young, The marvels of moiré materials, Nature Reviews Materials 2021 6:3 **6**, 201 (2021).

[3] R. Bistritzer and A. H. MacDonald, Moiré bands in twisted double-layer graphene, Proceedings of the National Academy of Sciences of the United States of America **108**, 12233 (2011), arXiv:1009.4203.

[4] Y. Cao, V. Fatemi, A. Demir, S. Fang, S. L. Tomarken, J. Y. Luo, J. D. Sanchez-Yamagishi, K. Watanabe, T. Taniguchi, E. Kaxiras, R. C. Ashoori, and P. Jarillo-Herrero, Correlated insulator behaviour at half-filling in magic-angle graphene superlattices, Nature 2018 556:7699 **556**, 80 (2018), arXiv:1802.00553.

[5] Y. Cao, V. Fatemi, S. Fang, K. Watanabe, T. Taniguchi, E. Kaxiras, and P. Jarillo-Herrero, Unconventional superconductivity in magic-angle graphene superlattices, Nature 2018 556:7699 **556**, 43 (2018).

[6] M. Yankowitz, S. Chen, H. Polshyn, Y. Zhang, K. Watanabe, T. Taniguchi, D. Graf, A. F. Young, and C. R. Dean, Tuning superconductivity in twisted bilayer graphene, Science **363**, 1059 (2019), arXiv:1808.07865.

[7] Y. Choi, J. Kemmer, Y. Peng, A. Thomson, H. Arora, R. Polski, Y. Zhang, H. Ren, J. Alicea, G. Refael, F. von Oppen, K. Watanabe, T. Taniguchi, and S. Nadj-Perge, Electronic correlations in twisted bilayer graphene near the magic angle, Nature Physics 2019 15:11 **15**, 1174 (2019), arXiv:1901.02997.

[8] N. Bultinck, E. Khalaf, S. Liu, S. Chatterjee, A. Vishwanath, and M. P. Zaletel, Ground state and hidden symmetry of magic-angle graphene at even integer filling, Phys. Rev. X **10**, 031034 (2020).

[9] Y. Xie, A. T. Pierce, J. M. Park, D. E. Parker, E. Khalaf, P. Ledwith, Y. Cao, S. H. Lee, S. Chen, P. R. Forrester, K. Watanabe, T. Taniguchi, A. Vishwanath, P. Jarillo-Herrero, and A. Yacoby, Fractional Chern insulators in magic-angle twisted bilayer graphene, Nature 2021 600:7889 **600**, 439 (2021), arXiv:2107.10854.

[10] Z.-D. Song and B. A. Bernevig, Magic-angle twisted bilayer graphene as a topological heavy fermion problem, Phys. Rev. Lett. **129**, 047601 (2022).

[11] C. Wang, X. Shen, R. Guo, W. Duan, C. Wang, and Y. Xu, Fractional chern insulators in moiré flat bands with high chern numbers, Physical Review B **112**, L201109 (2025).

[12] Z. Chen, N. Liu, J. Hua, H. Xiang, W. Zhou, J. Ding, X. Fang, L. Wu, L. Zhang, Q. Chen, X. Chen, K. Watanabe, T. Taniguchi, N. Xin, W. Zhu, and S. Xu, Layer-engineered quantum anomalous hall effect in twisted rhombohedral graphene family, arXiv:2601.14014 10.48550/arXiv.2601.14014 (2026), arXiv:2601.14014.

[13] R. Su, D. Waters, B. Zhou, K. Watanabe, T. Taniguchi, Y.-H. Zhang, M. Yankowitz, and J. Folk, Moiré-driven topological electronic crystals in twisted graphene, Nature **637**, 1084 (2025).

[14] C. Shen, Y. Chu, Q. Wu, N. Li, S. Wang, Y. Zhao, J. Tang, J. Liu, J. Tian, K. Watanabe, *et al.*, Correlated states in twisted double bilayer graphene, Nature Physics **16**, 520 (2020).

[15] H. Polshyn, J. Zhu, M. A. Kumar, Y. Zhang, F. Yang, C. L. Tschirhart, M. Serlin, K. Watanabe, T. Taniguchi, A. H. MacDonald, *et al.*, Electrical switching of magnetic order in an orbital chern insulator, Nature **588**, 66 (2020).

[16] H. Polshyn, Y. Zhang, M. A. Kumar, T. Soejima, P. Ledwith, K. Watanabe, T. Taniguchi, A. Vishwanath, M. P. Zaletel, and A. F. Young, Topological charge density waves at half-integer filling of a moiré superlattice, Nature Physics **18**, 42 (2022).

[17] S. Chen, M. He, Y.-H. Zhang, V. Hsieh, Z. Fei, K. Watanabe, T. Taniguchi, D. H. Cobden, X. Xu, C. R. Dean, *et al.*, Electrically tunable correlated and topological states in twisted monolayer–bilayer graphene, Nature Physics **17**, 374 (2021).

[18] M. He, Y. Li, J. Cai, Y. Liu, K. Watanabe, T. Taniguchi, X. Xu, and M. Yankowitz, Symmetry breaking in twisted double bilayer graphene, Nature Physics **17**, 26 (2021).

[19] X. Liu, Z. Hao, E. Khalaf, J. Y. Lee, Y. Ronen, H. Yoo, D. Haei Najafabadi, K. Watanabe, T. Taniguchi, A. Vishwanath, *et al.*, Tunable spin-polarized correlated states in

twisted double bilayer graphene, Nature **583**, 221 (2020).
[20] G. W. Burg, J. Zhu, T. Taniguchi, K. Watanabe, A. H. MacDonald, and E. Tutuc, Correlated insulating states in twisted double bilayer graphene, Physical review letters **123**, 197702 (2019).
[21] S. Xu, M. M. Al Ezzi, N. Balakrishnan, A. Garcia-Ruiz, B. Tsim, C. Mullan, J. Barrier, N. Xin, B. A. Piot, T. Taniguchi, *et al.*, Tunable van hove singularities and correlated states in twisted monolayer–bilayer graphene, Nature Physics **17**, 619 (2021).
[22] J. Y. Lee, E. Khalaf, S. Liu, X. Liu, Z. Hao, P. Kim, and A. Vishwanath, Theory of correlated insulating behaviour and spin-triplet superconductivity in twisted double bilayer graphene, Nature communications **10**, 5333 (2019).
[23] L. Rademaker, I. V. Protopopov, and D. A. Abanin, Topological flat bands and correlated states in twisted monolayer-bilayer graphene, Physical Review Research **2**, 033150 (2020).
[24] P. Wilhelm, T. Lang, M. S. Scheurer, and A. Läuchli, Non-coplanar magnetism, topological density wave order and emergent symmetry at half-integer filling of moiré chern bands, SciPost Physics **14**, 040 (2023).
[25] Z. Lu, T. Han, Y. Yao, A. P. Reddy, J. Yang, J. Seo, K. Watanabe, T. Taniguchi, L. Fu, and L. Ju, Fractional quantum anomalous hall effect in multilayer graphene, Nature **626**, 759 (2024).
[26] M. Song and K. Chang, Fractional chern insulators transition in non-ideal flat bands of twisted mono-bilayer graphene, arXiv preprint arXiv:2511.12231 (2025).
[27] D. Waters, A. Okounkova, R. Su, B. Zhou, J. Yao, K. Watanabe, T. Taniguchi, X. Xu, Y.-H. Zhang, J. Folk, and M. Yankowitz, Chern insulators at integer and fractional filling in moiré pentalayer graphene, Physical Review X **15**, 011045 (2025).
[28] J. Xie, Z. Huo, X. Lu, Z. Feng, Z. Zhang, W. Wang, Q. Yang, K. Watanabe, T. Taniguchi, K. Liu, Z. Song, X. C. Xie, J. Liu, and X. Lu, Tunable fractional chern insulators in rhombohedral graphene superlattices, Nature Materials **24**, 1042 (2025).
[29] V. T. Phong and C. Lewandowski, Coulomb interaction-stabilized isolated narrow bands with chern numbers $c > 1$ in twisted rhombohedral trilayer-bilayer graphene, arXiv preprint arXiv:2505.07981 (2025).
[30] Z. Wang, Y. H. Kwan, G. Wagner, S. H. Simon, N. Bultinck, and S. Parameswaran, Chern-textured exciton insulators with valley spiral order in moiré materials, Physical Review B **112**, 035130 (2025).
[31] Y. H. Kwan, Z. Wang, G. Wagner, S. H. Simon, S. Parameswaran, and N. Bultinck, Textured exciton insulators, Physical Review B **112**, 035129 (2025).
[32] J. Park, M. Luo, L. Rademaker, J. Smet, M. S. Scheurer, and L. Classen, Tuning correlated states of twisted mono-bilayer graphene with proximity-induced spin-orbit coupling, arXiv preprint arXiv:2603.10914 (2026).
[33] H. Zhang, J. Lu, K. Liu, Y. Wang, F. Wang, S. Wu, W. Chen, X. Cai, K. Watanabe, T. Taniguchi, J. Avila, P. Dudin, M. D. Watson, A. Louat, T. Sato, P. Yu, W. Duan, Z. Song, G. Chen, and S. Zhou, Moiré enhanced flat band in rhombohedral graphene, Nature Materials **25**, 566 (2026).
[34] Z. Li, W. Wang, F. Wang, Z. Zhang, Q. Yang, K. Watanabe, T. Taniguchi, X. C. Xie, J. Wang, K. Liu, Z. Song, and X. Lu, Fractional high-Chern insulator in twisted rhombohedral graphene, Nature **655**, 892 (2026).
[35] N. Liu, Z. Chen, J. Ding, W. Zhou, H. Xiang, X. Fang, L. Wu, X. Zhan, L. Zhang, Q. Chen, K. Watanabe, T. Taniguchi, N. Xin, and S. Xu, Diverse high-Chern-number quantum anomalous hall insulators in twisted rhombohedral graphene, arXiv:2507.11347 10.48550/arXiv.2507.11347 (2025), arXiv:2507.11347.
[36] X. Wang, L. A. Benítez, S. Rao, V. T. Phong, W. I. Chu, K. Watanabe, T. Taniguchi, C. Lewandowski, and P. Jarillo-Herrero, High-Chern-number orbital magnetism in twisted rhombohedral graphene, Nature Materials 10.1038/s41563-026-02659-7 (2026).
[37] P. San-Jose and E. Prada, Helical networks in twisted bilayer graphene under interlayer bias, Phys. Rev. B **88**, 121408 (2013).
[38] D. K. Efimkin and A. H. MacDonald, Helical network model for twisted bilayer graphene, Phys. Rev. B **98**, 35404 (2018).
[39] J. Li, K. Wang, K. J. McFaul, Z. Zern, Y. Ren, K. Watanabe, T. Taniguchi, Z. Qiao, and J. Zhu, Gate-controlled topological conducting channels in bilayer graphene, Nature Nanotechnology 2016 11:12 **11**, 1060 (2016), arXiv:1509.03912.
[40] S. Huang, K. Kim, D. K. Efimkin, T. Lovorn, T. Taniguchi, K. Watanabe, A. H. MacDonald, E. Tutuc, and B. J. LeRoy, Topologically Protected Helical States in Minimally Twisted Bilayer Graphene, Phys. Rev. Lett. **121**, 37702 (2018).
[41] C. De Beule, F. Dominguez, and P. Recher, Network model and four-terminal transport in minimally twisted bilayer graphene, Physical Review B **104**, 195410 (2021), arXiv:2107.04812.
[42] C.-H. Hsu, D. Loss, and J. Klinovaja, General scattering and electronic states in a quantum-wire network of moiré systems, Phys. Rev. B **108**, L121409 (2023).
[43] H.-C. Wang and C.-H. Hsu, Electrically tunable correlated domain wall network in twisted bilayer graphene, 2D Mater. **11**, 035007 (2024).
[44] N. C. Georgoulea, N. M. Caffrey, and S. R. Power, One-dimensional topological channels in heterostrained bilayer graphene, Phys. Rev. B **109**, 035403 (2024).
[45] Z. Hou, K. Yuan, and H. Jiang, Arrays of one-dimensional conducting channels in minimally twisted bilayer graphene, Phys. Rev. B **110**, L161406 (2024).
[46] J. Park, L. Gresista, S. Trebst, A. Rosch, and J. Park, Network of chiral one-dimensional channels and localized states emerging in a moiré system, 2D Materials **10**, 035033 (2023).
[47] R. Jackiw and C. Rebbi, Solitons with fermion number $\frac{1}{2}$, Phys. Rev. D **13**, 3398 (1976).
[48] J. Jung and A. H. MacDonald, Accurate tight-binding models for the π bands of bilayer graphene, Phys. Rev. B **89**, 035405 (2014).
[49] S. Carr, S. Fang, Z. Zhu, and E. Kaxiras, Exact continuum model for low-energy electronic states of twisted bilayer graphene, Phys. Rev. Research **1**, 013001 (2019).
[50] N. R. Walet and F. Guinea, The emergence of one-dimensional channels in marginal-angle twisted bilayer graphene, 2D Mater. **7**, 015023 (2020).
[51] L. Rademaker, I. V. Protopopov, and D. A. Abanin, Topological flat bands and correlated states in twisted monolayer-bilayer graphene, Phys. Rev. Res. **2**, 033150 (2020).